Field dependent transition to the non-linear regime in magnetic hyperthermia experiments: Comparison between maghemite, copper, zinc, nickel and cobalt ferrite nanoparticles of similar sizes

E. L. Verde,[1,2] G. T. Landi,[3] M. S. Carrião,[1] A. L. Drummond,[4] J. A. Gomes,[5] E. D. Vieira,[1] M. H. Sousa,[4] and A. F. Bakuzis[1,a]

[1]*Universidade Federal de Goiás, Instituto de Física, 74001-970, Goiânia-GO, Brazil*
[2]*Universidade Federal de Mato Grosso, Instituto de Ciências Exatas e da Terra, 3500, Pontal do Araguaia-MT, Brazil*
[3]*Universidade de São Paulo, Instituto de Física, 05314-970, São Paulo-SP, Brazil*
[4]*Universidade de Brasília, Faculdade de Ceilândia, 72220-140, Brasília-DF, Brazil*
[5]*Instituto de Criminalística, Polícia Civil do Distrito Federal, 70610-200, Brasília-DF, Brazil*

(Received 3 February 2012; accepted 13 July 2012; published online 20 July 2012)

Further advances in magnetic hyperthermia might be limited by biological constraints, such as using sufficiently low frequencies and low field amplitudes to inhibit harmful eddy currents inside the patient's body. These incite the need to optimize the heating efficiency of the nanoparticles, referred to as the specific absorption rate (SAR). Among the several properties currently under research, one of particular importance is the transition from the linear to the non-linear regime that takes place as the field amplitude is increased, an aspect where the magnetic anisotropy is expected to play a fundamental role. In this paper we investigate the heating properties of cobalt ferrite and maghemite nanoparticles under the influence of a 500 kHz sinusoidal magnetic field with varying amplitude, up to 134 Oe. The particles were characterized by TEM, XRD, FMR and VSM, from which most relevant morphological, structural and magnetic properties were inferred. Both materials have similar size distributions and saturation magnetization, but strikingly different magnetic anisotropies. From magnetic hyperthermia experiments we found that, while at low fields maghemite is the best nanomaterial for hyperthermia applications, above a critical field, close to the transition from the linear to the non-linear regime, cobalt ferrite becomes more efficient. The results were also analyzed with respect to the energy conversion efficiency and compared with dynamic hysteresis simulations. Additional analysis with nickel, zinc and copper-ferrite nanoparticles of similar sizes confirmed the importance of the magnetic anisotropy and the damping factor. Further, the analysis of the characterization parameters suggested core-shell nanostructures, probably due to a surface passivation process during the nanoparticle synthesis. Finally, we discussed the effect of particle-particle interactions and its consequences, in particular regarding discrepancies between estimated parameters and expected theoretical predictions. [http://dx.doi.org/10.1063/1.4739533]

I. INTRODUCTION

Cubic ferrite nanoparticles are known to have several technological applications due to the possibility of modifying their magnetic properties through cation distribution or atom substitution into the tetrahedral or octahedral crystallographic sites.[1–4] Their basic formula is $M^{2+}Fe_2{}^{3+}O_4{}^{2-}$,

[a]Corresponding author. E-mail: bakuzis@if.ufg.br

where M is a divalent atom (ex.: Fe^{2+}, Co^{2+}, Zn^{2+}, Ni^{2+}, etc). Besides technological applications in spin-filtering[5] and multiferroic devices,[6,7] several biomedical applications on targeting, diagnosis and disease treatment have been reported. These are usually related to the fact that nanoparticles are excellent contrast agents in nuclear magnetic resonance imaging and, as a consequence, are already being used for stem cell labeling, atherosclerosis and metastasis detection. In addition, several other novel potential applications have been proposed over the past few decades concerning, in particular, cancer treatment through the delivery of drugs, genes, peptides or *heat*.[8–17]

The heating of tumorous cells is based upon the magnetic hyperthermia phenomenon, which consists of an increase in the temperature of magnetic nanoparticles due to the interaction of their magnetic moments with an alternating magnetic field. Recently, there has been a considerable effort from the community to develop more efficient heating centers. Unfortunately, besides biocompatibility issues, there is also another very important constraint, namely, the frequency and magnitude of the alternating magnetic field need to be lower than a critical value in order to inhibit possibly harmful eddy currents in the patient's body.[18] Therefore, the success of this application requires a deep understanding of the magnetic properties of the nanoparticles and how these are influenced by the external stimuli.

In this paper we investigate the magnetic hyperthermia properties of cobalt-ferrite ($CoFe_2O_4$), maghemite (γ-Fe_2O_3), nickel-ferrite ($NiFe_2O_4$), zinc-ferrite ($ZnFe_2O_4$), and copper-ferrite ($CuFe_2O_4$) nanoparticles of similar sizes. The distinct values of the magnetic anisotropy of the ferrite-based nanoparticles allowed us to investigate the main effects of this important parameter. Specific Absorption Rate (SAR; power dissipated per unit mass) data for applied magnetic fields up to 134Oe were obtained and compared with analytical predictions from the linear response theory (LRT), as well as with numerical simulations of dynamic hysteresis (DH) using the stochastic Landau-Lifshitz equation. Our main goal is to investigate in detail the relation between the anisotropy and the magnetic field amplitude on the hyperthermia phenomenon. From our viewpoint, this information is of crucial importance for the development of more efficient magnetic hyperthermia nanostructures. The strategy of this article will be, firstly, to compare two very distinct samples with respect to the DC coercivity, namely the cobalt-ferrite and the maghemite ones. Then, introduce data of the other ferrite-based nanoparticles in order to definitely prove the role of magnetic anisotropy to the magnetic hyperthermia properties of the magnetic nanoparticles.

As far as we know, the first group of scientists to propose the use of magnetic nanoparticles for cancer treatment dates back to the 1950's, where Gilchrist *et al.*[8] already pointed out to the possibility of three contributions to the heating phenomena, namely dielectric losses, eddy current losses and hysteresis losses. Although new magnetic materials for this application are still under research, most papers now focus on ferrite-based nanoparticles due to its biocompatibility. In this type of material the first two contributions are believed to be negligible. Moreover, sufficiently small particles are likely to remain in a single-domain state, favoring coherent rotation as the dominant hysteresis loss mechanism. At sufficiently low field amplitudes the response is expected to be linear, yielding ellipsoidal hysteresis loops. In this case, if we assume (as usually is) only a single relaxation mode, then the average power loss is given by[15,19]

$$P_m^{LRT} = \pi \mu_0 \chi_0 H_0^2 f \frac{2\pi f \tau}{1 + (2\pi f \tau)^2}, \tag{1}$$

Where χ_0 is the equilibrium susceptibility and $\tau = \tau_0(\pi/4\sigma)^{1/2} e^{\sigma}$ is the Néel-Brown relaxation time,[20] with $\tau_0 = (\gamma \mathrm{H_A})^{-1} \sim 10^{-12} - 10^{-8} s$ and $\sigma = K_{eff}\mathrm{V/kT}$. Here $\mathrm{H_A} = 2K_{eff}/M_s$, K_{eff} is the effective magnetic anisotropy, $\gamma = \frac{\gamma_0}{1+\alpha^2}$, γ_0 is the gyromagnetic ratio of the electron, α is the damping constant, M_s is the saturation magnetization, V is the particle's volume, k is Boltzmann's constant and T is the sample temperature.

Note that in the linear regime $P_m^{LRT} \propto \mathrm{H_0^2}$. This should actually be interpreted as an asymptotic behavior for sufficiently small fields. There is also an interesting physical interpretation stemming from this relation since $\mathrm{H_0^2}$ is proportional to the electromagnetic energy density in the vicinity of the nanoparticles. Thus, magnetic hyperthermia may be analyzed with respect to the conversion from electromagnetic to thermal energy.[21] We define the efficiency of conversion as $\Omega = P_m^{LRT}/\mathrm{H_0^2}$ (or, equivalently, $\Omega = SAR/\mathrm{H_0^2}$). Apart from its physical interpretation, this parameter is actually

quite useful in the analysis of experimental data, in particular on the initial departure towards the non-linear regime as the field amplitude is gradually increased. The reason for this is as follows. The power loss, which is the true quantity of interest, must always increase with H_0 (eventually saturating at high enough fields). Quantifying this dependence is thus not trivial. On the other hand, it is far more convenient to use the efficiency since it may either increase or decrease, tending to a constant value at sufficiently small fields.

The following heuristic argument may be used to infer which response one should roughly expect from the efficiency. The condition that the measurement time matches the relaxation time is given by some value σ_{max} which satisfies $f\tau = 1$. Systems with $\sigma < \sigma_{max}$ are characterized by a low barrier regime where arbitrarily low fields already have a certain influence on the magnetization dynamics; whence the efficiency in this region should decrease as the field increases. Conversely, $\sigma > \sigma_{max}$ denotes a high barrier condition where the spins are "frozen" near the energy minima causing small fields to have a negligible influence on their motion. Increasing the field gradually "unfreezes" the particles and consequently the efficiency is expected to increase. Since the power loss saturates, such increase must be followed by a maximum, after which the efficiency tends to zero asymptotically. We also emphasize that the terms "high" and "low" barrier are related to the frequency of the external field, in the present case ∼500 kHz. The value of $\sigma_{\max}$ for quasi-static measurements is obviously different (in the literature one often sees $\sigma_{max} \sim 25$ in this case). Both parameters, SAR and Ω, will be extensively investigated in this work.

II. SAMPLE SYNTHESIS AND CHARACTERIZATION

The ferrite nanoparticles nanoparticles were synthesized by forced hydrolysis of Fe^{3+} and M^{2+} (M = Co, Cu, Ni and Zn) using a procedure adapted from reference 22 for cobalt ferrite and from reference 23 for copper, nickel and zinc ferrites. In this process, 50 mL of a stoichiometric Fe^{3+}/M^{2+} solution, containing 25 mmol of Fe^{3+}, reacted with 200 mL of 2 mol/L NaOH solution at boiling temperature under vigorous stirring for 60 minutes. After synthesis, each obtained solid was magnetically separated from the supernatant and washed three times with distilled water. After that, the precipitate was acidified with a 2mol/L HNO_3 solution and the supernatant discarded. The nanograins were hydrothermally treated by boiling 1mol/L $Fe(NO_3)_3$ for 30 minutes and the excess of ferric nitrate was removed from the solution by magnetic decantation. The precipitate was then directly peptized in aqueous acidic medium according to the procedure reported. In this case, the nanograins were washed with acetone three times, then the desired amount of water was added and the excess of acetone evaporated in order to form a magnetic fluid with $pH \sim 2$.

Magnetite (Fe_3O_4) nanoparticles were synthesized using chloride salts of Fe^{3+} and Fe^{2+}. A 100 mL stoichiometric solution of Fe^{3+}/Fe^{2+} was dropped into a 100 mL containing 1.5 mol/L of NaOH solution under vigorous stirring for 25 minutes. The obtained solid was then magnetically separated from the supernatant and washed with distilled water until a neutral pH was obtained. Afterwards, HCl was gradually added to the solution containing the precipitate until a pH of 3.5 was reached. Then 25 mL of a solution containing 0.15 mol/L of tripolyphosphate ($Na_5P_3O_{10}$) was added, which configured the surface coating layer of the magnetite nanoparticles. After 24 hours of mechanical agitation and subsequent dialysis a stable magnetic fluid of magnetite nanoparticles coated with tripolyphosphate at physiological pH was finally obtained. In order to check if the nanoparticle was actually magnetite X-ray diffraction and titration was obtained.

The X-ray powder diffractograms of the synthesized sample and patterns of magnetite and maghemite bulk standards are shown in Fig. 1(a). In fact, as observed in diffractograms of standard magnetite and maghemite samples, the juncture of peaks present in diffractograms of magnetite and maghemite is very analogous, except that peaks slightly dislocate towards the right from Fe_3O_4 to γ-Fe_2O_3. Thus, after indexing the main peaks using Bragg's law and comparing them to the ASTM standards, the most probably structure to the synthesized sample is maghemite, but with a little amount of magnetite. According to the chemical reaction that describes the formation of magnetite, $Fe^{2+} + 2Fe^{3+} + 8OH^- \rightarrow Fe_3O_4 + 4H_2O$, an initial molar ratio of Fe^{3+}:Fe^{2+}= 2:1 is needed for the production of Fe_3O_4. However, when the preparation is carried out in air or another oxidizing environment, it is very difficult to maintain this ratio at 2:1, because Fe^{2+} is oxidized to Fe^{3+} and

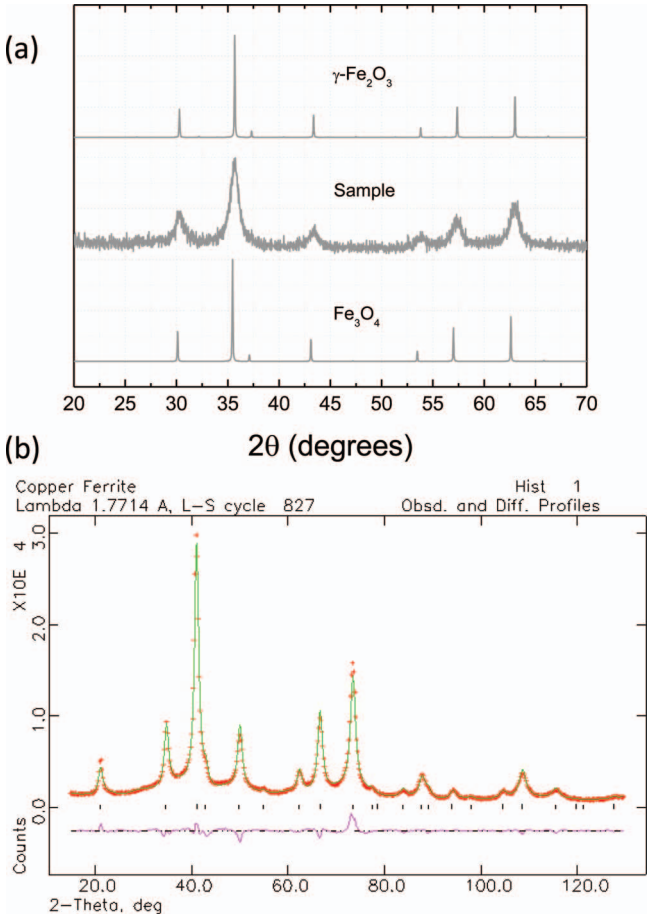

FIG. 1. (a) The X-ray powder diffractograms of the synthesized sample and patterns of magnetite and maghemite bulk standards. (b) Rietveld refinement pattern of the copper-ferrite sample. The lower curve represents the difference between the observed and calculated profiles. Plus (+) marks represent the collected data and tic marks show the positions for the allowed reflections. The agreement factors for X-ray diffraction obtained from the Rietveld analysis were: Rp = 4.42%, Rwp = 5.69% and $\chi 2 = 9.454$.

magnetite is converted to maghemite according to the reaction: $2Fe_3O_4 + \frac{1}{2}O_2 \rightarrow \gamma\text{-}Fe_2O_3$. So, in order to finally verify the nanomaterial structure we analysed the sample from chemical dosages, which revealed that the amount of magnetite in this sample was estimated to be only 5.5%. Therefore, from now on, the sample will be named maghemite.

Cobalt ferrite transmission electron microscopy (TEM) micrographs were obtained using a JEOL 1100 microscope operating at 80 kV, while for maghemite we used a JEOL JEM-3010 ARP microscope operating at 300kV (resolution 1.7Å). Fig. 2(b) (Fig. 2(d)) shows a typical TEM picture of the cobalt ferrite (maghemite) nanoparticles, where the scale bar is 50 nm (10 nm). The corresponding size distribution histograms are shown in Figs. 2(a) and 2(c), along with the corresponding fits for a lognormal size distribution function, $P(D) = 1/(\sqrt{2\pi} D\delta \exp\left[-\log^2(D/D_{TEM})/2\delta^2\right])$. The obtained fitted values were $D_{TEM} = 10.2$ nm and $\delta = 0.26$ for cobalt ferrite and $D_{TEM} = 9.2$ nm and $\delta = 0.24$ for maghemite. The insets in Figs. 2(b) and 2(d) also show the x-ray diffraction patterns confirming the spinel structure in both materials. The differences in the data intensity for both samples has to do with the fact that for the cobalt ferrite nanoparticles the measurements were performed on a synchrotron source at the Brazilian National Synchrotron Laboratory (LNLS) facility, whereas for maghemite we used a Shimadzu XRD 6000 spectrometer with CuK_α radiation. Note from the TEM pictures that the nanoparticles are not perfect spheres. Therefore a shape contribution to the magnetic anisotropy is expected.

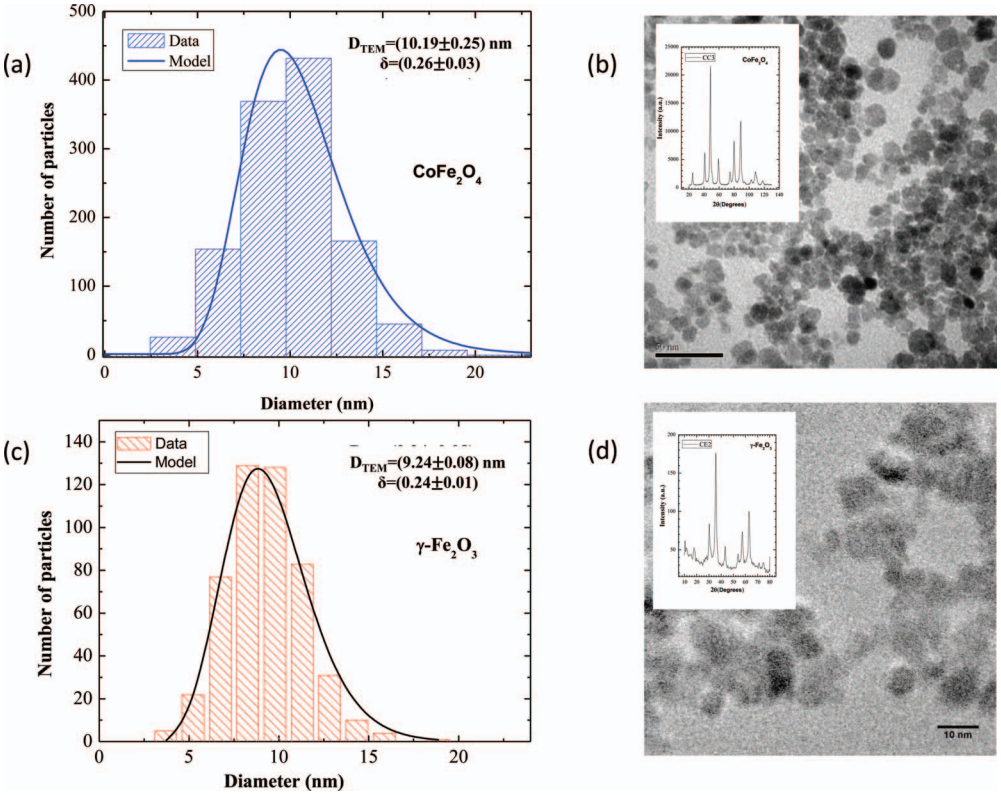

FIG. 2. Morphological characterization. TEM micrographs for cobalt ferrite (b) and maghemite (d); the inset illustrates data from X Ray diffraction. The corresponding size distribution histograms are shown in images (a) and (c) respectively, together with a lognormal distribution fit.

The room temperature x-ray powder diffraction patterns of the Cu, Ni and Zn ferrite samples were also measured at the Brazilian Synchrotron Light Laboratory (LNLS) using the D12A-XRD1 beam line. For these samples, however, the average diameter D_{RR} was estimated only from a Rietveld analysis. The sample holder is rotated to improve the randomization of the crystallites. Monochromatized 6.01 keV ($\lambda = 2.0633$ Å) X-ray beam of approximately 4 x 1.5 mm^2 area are used. Diffraction patterns are obtained typically within $20^\circ \leq 2\theta \leq 130^\circ$ interval, with 0.04° step and 7 seconds counting time. Fig. 1(b) exhibits a typical experimental x-ray diffraction pattern for the sample based on copper ferrite nanoparticles. For all the samples investigated here, the analysis of the peak positions and relative intensities of the diffracted lines confirms the presence of only one phase characteristic of the spinel crystallographic structure. The lattice parameter values, *a*, agree with those presented in the ASTM. The oxygen positional parameters, *u*, are slightly larger than the expected value for an ideal cubic close packed arrangement, equal to 0.25. One can remark that if a certain degree of inversion exists in ferrite nanocrystals, it would probably induce some distortion in the oxygen position depending on the divalent metal ionic radius. Table I shows the nanoparticle sizes obtained from the RT analysis. Indeed, the diameters of the samples are very close from one another, spanning from 9.0 to 9.4 nm (well within experimental error). Moreover, the degree of cation distribution for all ferrites were exceptionally close to 1 (inverted spinel structure), the exception being the zinc-ferrite nanoparticle where x = 0.28. Thus, from this analysis we conclude that, both structurally and morphologically, all samples are indeed quite similar.

The room temperature nanoparticle magnetization characterization was obtained using an ADE vibrating sample magnetometer model EV7. Fig. 3(a) shows the magnetization curves for two powder samples, cobalt-ferrite and maghemite, with Fig. 3(b) being a magnification of the same curves at the low field range. Note that maghemite shows no hysteresis, while for cobalt ferrite we found a coercive field of 153Oe. The saturation magnetization values were obtained from data

TABLE I. Estimated parameters for cobalt, copper, nickel, zinc ferrite and maghemite nanoparticles. **Exp.** correspond to experimentally estimated values, while **Bulk** is related to calculations using the reported bulk values. M_S is the saturation magnetization, $\mathbf{H_C}$ the coercivity, $\mathbf{D_{RR}}$ the particle diameter estimated from Rietveld analysis, **x** the degree of cationic distribution, $\mathbf{H_R}$ the electron magnetic resonance field, $\delta\mathbf{H_R}$ the resonance linewidth, $\mathbf{D_{TEM}}$ modal diameter and $\delta_\mathbf{D}$ size dispersity from Log-normal size distribution, α the damping factor, K_{eff} effective magnetic anisotropy, σ_{dip} dipolar anisotropy parameter, σ anisotropy parameter, H_A anisotropy field, τ_0 characteristic time, **f** magnetic field frequency and σ_{max} anisotropy parameter value with maximum hyperthermia. Values in brackets were estimated taking into account the polidispersity of the sample.

	$CoFe_2O_4$		γ-Fe_2O_3		$CuFe_2O_4$		$NiFe_2O_4$		$ZnFe_2O_4$	
	Exp.	Bulk	Exp.	Bulk	Exp.	Bulk	Exp.	Bulk	Exp.	Bulk
M_s (emu/cm^3)	271.9	425	209.1	417	124.2	135	153.7	270	219.8	-
$\mathbf{H_c}$ (Oe)	152		2.7		0.5		1.1		0.3	
D_{RR} (nm)	9.1		*9.3		9.4		9.2		9.0	
x	0.99		-		0.99		0.99		0.28	
$\mathbf{H_R}$ (Oe)	-		3192		3001		2793		2893	
$\delta\mathbf{H_R}$ (Oe)	-		723		782		1089		235	
$\mathbf{D_{TEM}}$ (nm)	10.2		9.2		-		-		-	
$\delta_\mathbf{D}$	0.26		0.24		-		-		-	
α	1.0		0.05		0.06		0.09		0.02	
K_{eff} ($\times 10^5$ erg/cm3)	3.7	18	0.2	0.5	0.2	-	0.4	0.7	0.5	-
σ_{dip} (Eq. (5))	3.7 [7.0]	9.0 [17.2]	2.3 [2.9]	9.3 [11.6]	0.8	-	1.2	1.2	2.3	-
$\sigma = K_{eff}V/kT$	3.5 [6.7]	17.2 [32.7]	0.2 [0.2]	0.5 [1.3]	0.2	-	0.4	0.7	0.5	-
$H_A = 2K_{eff}/M_s$ (Oe)	2721	8470	173	240	364	-	572	911	472	-
$\tau_0 = \frac{(1+\alpha^2)}{\alpha\gamma_0 H_A}$ (sec)	4.2 $\times 10^{-11}$	1.3 $\times 10^{-11}$	6.6 $\times 10^{-9}$	4.7 $\times 10^{-9}$	2.6 $\times 10^{-9}$	-	1.1 $\times 10^{-9}$	7.0 $\times 10^{-10}$	6.0 $\times 10^{-9}$	-
$\mathbf{f}\tau_\mathbf{0}$	2.1 $\times 10^{-5}$	6.7 $\times 10^{-6}$	3.3 $\times 10^{-3}$	2.3 $\times 10^{-3}$	1.3 $\times 10^{-3}$	-	5.6 $\times 10^{-4}$	3.5 $\times 10^{-4}$	3.0 $\times 10^{-3}$	-
$\sigma_{max}(f\tau = 1)$	11.5	12.7	6.2	6.5	7.2	-	8.1	8.6	6.3	-

extrapolation at the high-field limit, from which we found 49 and 41 emu/g for cobalt ferrite and maghemite nanoparticles, respectively. For DC superparamagnetic particles one just need to expand the Langevin function at the high-field limit. So from the fitting of the data, at this regime, one extracts the saturation magnetization value. Although, not shown the particle concentrations for the magnetic colloids of those samples were also obtained from magnetization analysis.

It is well known that the magnetic anisotropy of both materials is very different. For instance, the bulk cobalt ferrite cubic anisotropy is $K_{bulk}^{Co} = 1.8x10^6 erg/cm^3$, while for maghemite one finds[15] $K_{bulk}^{Fe} = 0.5x10^5 erg/cm^3$. Moreover, the anisotropy in nanoparticles usually differ significantly from its bulk counterpart due to surface effects or magnetostatic and magnetoelastic contributions.[24–26] Our strategy to estimate the anisotropy values of the samples was as follows: for the maghemite (as well as for copper, zinc and nickel-ferrite) nanoparticles we measured the electron magnetic resonance at the X-band using a Bruker ESP-300 equipment tuned at $\nu = 9.43$GHz (see the inset in Fig. 3(b)). The effective uniaxial magnetic anisotropy was obtained neglecting particle-particle interactions (as a first-order approximation) from[27]

$$K_{eff} = \frac{M_S}{2}\left(\frac{2\pi\nu}{\gamma_0} - H_R\right), \tag{2}$$

where H_R is the resonance field. From this analysis we found for maghemite K_{eff}^{Fe} =6.1x10^{4}erg/cm^3. In addition, we assumed the damping factor of maghemite to be $\alpha_{Fe} \sim 0.05$. Note in the inset of Fig. 3(b) that we also measured the ferromagnetic resonance spectra of the cobalt ferrite sample.

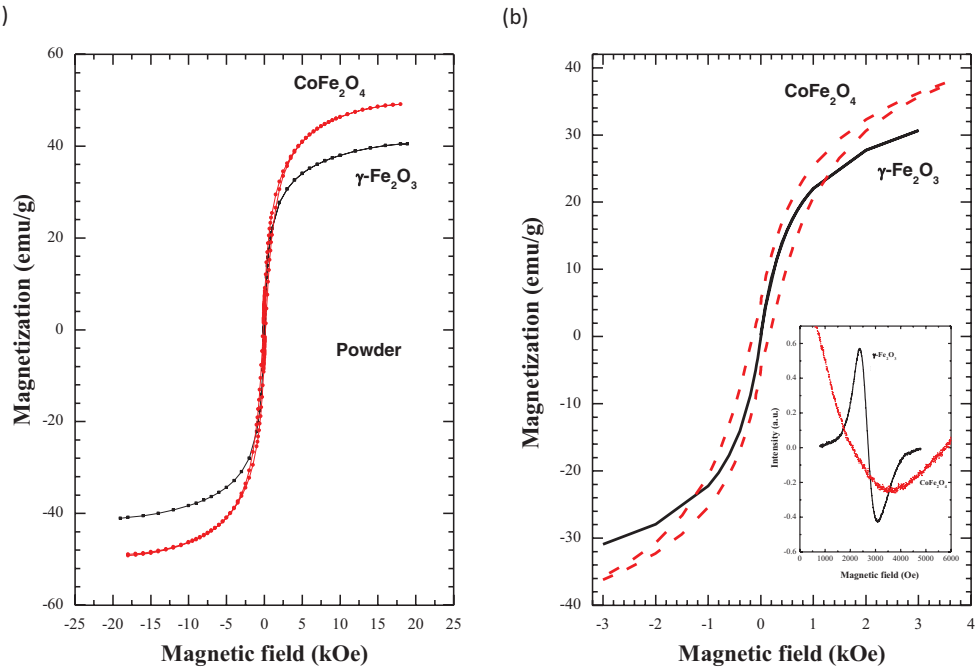

FIG. 3. (a) Vibrating sample magnetometry for cobalt ferrite and maghemite nanoparticles. (b) Magnification of image (a) at small fields. The inset in Fig. 2(b) shows ferromagnetic resonance data for both samples, measured at the X-band.

Clearly, no information may be extracted from such data, which is severely broadened. Besides the magnetic anisotropy, this is likely caused by the larger damping factor (henceforth taken as $\alpha_{Co} \sim 1$). As a consequence, the cobalt ferrite anisotropy was obtained considering a three-dimensional random anisotropy axis coercivity[28] (H_c^{3D}) taking into account particle interactions.[29] In this case the experimental coercive field is equal to the isolated nanoparticle coercivity[28] (H_c^{3D}) times an interaction term which is proportional to the packing fraction (p) of the nanoparticles,[29] $H_c = H_c^{3D}(1-p)$. Note that this expression is valid whenever shape anisotropy is dominant, which according to our TEM picture is a good assumption. So K_{eff} can be calculated from

$$K_{eff} = \frac{M_s * H_c}{0.96 * [1 - \left(\frac{D_{sp}}{d}\right)^{2.25}](1-p)}. \quad (3)$$

where D_{SP} is the superparamagnetic diameter, which was found to be ~7nm from a complete size data analysis using different samples (data not shown; see Ref. 31). In passing, we note that this equation is only valid for particles with sizes larger than D_{SP}. Let us comment briefly on the expected value of the packing fraction, (p). For spherical particles, one would usually expect it to lie between 0.634, which is the value for the random close packing of spheres, and 0.659 corresponding to the unequal sphere packing of a bidisperse system. However, for ellipsoidal shapes, this is expected to remain a good approximation only for slightly anisometric ellipsoids, with an aspect ratio no larger than 1.1. Moreover, according to a recent study,[30] the packing fraction can increase significantly with the aspect ratio, reaching values as large as $p \sim 0.74$. Given the importance this may have in the analysis of the cobalt ferrite sample, we analyzed roughly 150 particles from our TEM images. The result was an aspect ratio of 1.25 ± 0.31. Whence, considering that the nanoparticles have an aspherical shape, according to Ref. 30, we considered p = 0.74. We also note that, if we were to use p = 0.64, the anisotropy of the cobalt ferrite sample would be lowered by a factor of roughly 30% (see Ref. 31). Now, returning to Eq. (3), we find from this analysis $K_{eff}^{Co} = 3.7\text{x}10^5 \text{erg/cm}^3$. Thus, as expected, the anisotropy of cobalt ferrite is higher than that of maghemite.

Further, room temperature ferromagnetic resonance spectra and quasi-static magnetization curves of all the powder samples are shown in Figs. 4(a) and 4(b) respectively. From Fig. 4(a)

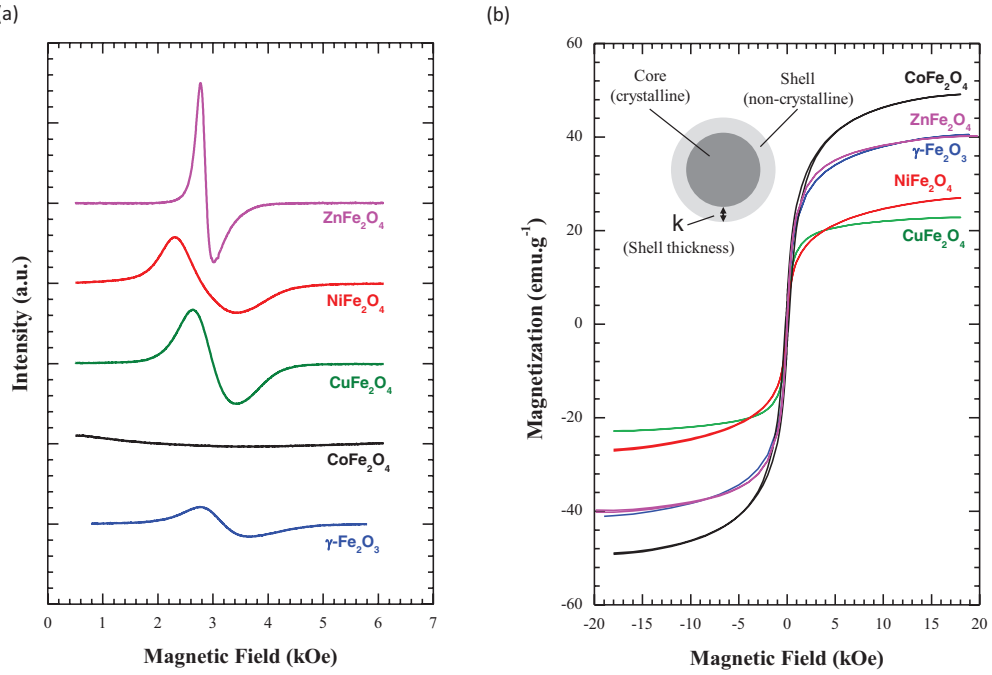

FIG. 4. (a) X-band room temperature ferromagnetic resonance spectra of the ferrite-based nanoparticles. (b) Quasi-static room temperature magnetization curves of all the powder samples. The inset shows a schematic representation of a core-shell nanoparticle.

it is clear that the resonance field is lower for the Zn nanoparticle and then gradually increases for Ni and Cu, until achieving the highest value for the maghemite nanoparticle. Here, is interesting to point that the resonance experimental conditions were, as discussed before, the same for all the nanoparticle samples (maghemite, copper-ferrite, nickel-ferrite and zinc-ferrite nanoparticles) with respect to the field and frequency modulation, as well as the microwave power. Nevertheless the mass used in this experiment was not the same, so one cannot extract any relevant information about the spectra intensity. As previously discussed, at this frequency (X-band) no information can be extracted for the cobalt-ferrite nanoparticles, due to both the high anisotropy and high damping factor. As before, using equation (2), we estimated the effective magnetic anisotropy of each sample. Moreover, the analysis of the data shown in Fig. 4(b) (at the high field limit) allowed us to extract the saturation magnetization of each nanoparticle. Table I presents the parameters extracted from all the characterization techniques for these new samples. It is important to point out that all the nanoparticles showed lower saturation magnetization values when compared to the bulk ones. In principle one would expect that this behavior could be related to a degree of cation redistribution in the spinel structure. However, from the Rietveld analysis, it is clear that most of the samples (cobalt-ferrite, copper-ferrite and nickel-ferrite) maintain the inverted spinel structure, i.e x=1 (see Table I). So this does not explain the magnetization data.

Indeed, the differences between the average diameter D_{RR} from Rietveld analysis and the TEM one D_{TEM} for the cobalt-ferrite sample can be explained in terms of a core-shell nanostructure consisting of a crystalline core and a magnetically weak non-crystalline shell (sometimes named in the literature as a "dead magnetic layer" – see the inset of Fig. 4(b)). The core diameter could be related to D_{RR}, while an estimate of the particle size comes from D_{TEM}. In particular, for cobalt-ferrite, from such analysis, one can estimate a shell thickness around 0.6 nm. Note, that the same approach cannot be done with the maghemite sample since we were not able to do Rietveld analysis due to the bad quality of the X-ray diffraction data. This means that the diameter for maghemite is not necessarily so "trustable" as the other samples, which have x-ray data from a synchrotron source. Also, besides the maghemite nanoparticle, all other samples had passed through a surface

TABLE II. Estimated parameters using the **core-shell model** for maghemite, copper, cobalt and nickel ferrite nanoparticles. CS-Diam correspond to calculations using the value of the core fraction (f_{core}) estimated from the combination of Rietveld and TEM analysis, while CS-Magn correspond to calculations using the core fraction estimated from magnetization data (see discussion in the text). Some parameters had already been defined in Table I, however others are defined as: M_s^{core} core magnetization, M_s^{part} experimentally determined particle magnetization, f_{core} fraction of core atoms, κ non-crystalline shell thickness, $^*\mathbf{D}_{\mathbf{MODAL}}$ modal particle size estimated from the core-shell model and $^*\delta_{\mathbf{D}}$ size dispersity assumed in the calculations of the relevant parameters.

	$CoFe_2O_4$		γ-Fe_2O_3	$CuFe_2O_4$	$NiFe_2O_4$
	CS-Diam.	CS-Magn.	CS-Magn.	CS-Magn.	CS-Magn.
M_s^{core} **(emu/cm^3)**	425		417	135	270
M_s^{part} **(emu/cm^3)**	271.9		209.1	124.2	153.7
D_{RR} **(nm)**	9.1		*9.3	9.4	9.2
α	1.0		0.05	0.06	0.09
$\mathbf{D}_{\mathbf{TEM}}$ (nm)	10.2		9.2	-	-
$\delta_{\mathbf{D}}$	0.26		0.24	-	-
f_{core}	0.71	0.64	0.49	0.86	0.54
κ **(nm)**	0.6	0.7	1.2	0.2	1.0
$^*\mathbf{D}_{\mathbf{MODAL}}$ **(nm)**	10.2	10.6	11.8	9.9	11.3
$^*\delta_{\mathbf{D}}$	0.26	0.26	0.24	0.25	0.25 (0.30)
K_{eff} **($\times 10^5$ erg/cm3)**	5.8	5.8	0.4	0.2	0.8
σ_{dip-CS} **(Eq. (6))**	15.9	14.4	9.9	2.0	4.7 (6.8)
$\sigma = K_{eff}V/kT$	10.5	11.7	1.0	0.4	1.9 (2.1)
$H_A = 2K_{eff}/M_s$ **(Oe)**	2729	2729	173	364	572
$\tau_0 = \frac{(1+\alpha^2)}{\alpha\gamma_0 H_A}$ **(sec)**	4.2×10^{-11}	4.2×10^{-11}	6.6×10^{-9}	2.6×10^{-9}	1.1×10^{-9}
$\mathbf{f}\tau_0$	2.1×10^{-5}	2.1×10^{-5}	3.3×10^{-3}	1.3×10^{-3}	5.6×10^{-4}
$\sigma_{max}(f\tau = 1)$	11.5	11.5	6.2	7.2	8.1

passivation process, whose objective is to prevent the nanoparticle degradation in acidic medium. During this synthesis step a weakly magnetic layer is formed at the nanoparticle surface, as found by other authors.[32] Further, in a recent paper of our group, using cobalt-ferrite nanoparticles of distinct sizes, a better representation of the hyperthermia experimental data, at low field amplitudes, was found considering the core-shell model.[31] Note that the same model can be used to explain the discrepancies between the measured magnetization values and the expected bulk ones. By assuming that the shell layer is very weakly magnetic (zero magnetization) and that the core has the same saturation magnetization as the bulk one can extract the fraction of atoms at the core region f_{core} (see Table II). Note that for cobalt-ferrite we obtained from the diameter analysis a value for f_{core} of *0*.71, while from the magnetization calculation one obtain 0.64. This means that the shell thickness calculated from the later procedure was found to be 0.7 nm, which is very close to the approach reported before 0.6 nm (Cs-Diam). Therefore, this approach could be used for the other samples as well, which we do not have the TEM data. The estimation of the shell thickness from the magnetization procedure is named CS-Magn. In Table II is shown the core fraction, as well as the shell thickness calculated using the core-shell model for all the ferrites, the exception being the zinc-based one which has a mixed spinel cation distribution and was not analysed within this framework. Note that the values found for the present samples are of the same order of others reported in the literature.[32] Also, in Table II, are the new values of other parameters when using the core-shell model. In particular, higher anisotropy values were found when compared with the homogeneous particle calculation (see Table I).

The magnetic anisotropy, particle size, damping factor and saturation magnetization values will be important in the analysis of the hyperthermia data and the dynamic hysteresis simulations discussed below. With them, it is also possible to compute other quantities of interest. These are shown in Table I together with the main results obtained in this section. Note that, by far, the largest uncertainty pertaining to our calculations lie in the values of K_{eff}, overshadowed by the inter-particle interactions; thus we also include the bulk values for comparison. As can be seen, the larger

anisotropy for the cobalt ferrite entails a significantly larger value for the anisotropy parameter, σ. Also, one can observe that the experimentally determined anisotropy of nickel-ferrite, when using the core-shell model, is higher than the corresponding bulk value. In fact, results from the literature already point out the importance of the nanoparticle surface in those type of ferrites due to broken exchange bonds and/or spin canting effects at the nanoparticle surface.[33,34] So a surface anisotropy contribution might play an even more relevant role here.[35]

Moreover, the marked difference in the values of the damping, coupled with the differences in the anisotropy, also yield considerably different values of τ_0. This parameter is of particular importance since it describes the characteristic time scale for the precession of the magnetization. Further, according to resonance theory,[27] the ferromagnetic resonance linewidth (δH) is proportional to the damping factor. As a consequence, the analysis of δH [see Table I, Table II, Fig. 4(a), and the inset of Fig. 3(b)] strongly suggests that cobalt-ferrite nanoparticles, besides having the largest anisotropy, also have an exceptionally large damping factor in comparison with the other ferrite-based nanoparticles. In addition, one might also approximately expect that the larger the linewidth, the higher the damping factor. Therefore, from the largest to the lower linewidth one would have the following order: Ni-ferrite > Cu-ferrite > maghemite > Zn-ferrite based nanoparticle. Indeed, a rough estimate can be made by using the relation between the linewidth, the damping factor and the effective magnetic field felt by the electrons at each nanoparticle, $\delta H_R = \alpha H_{ef}$, which we assume is proportional to the resonance field. Thus in this case the ratio between the damping factor of a ferrite-based nanoparticle (α_i) to the maghemite (α_{Fe}) one can be found from

$$\frac{\alpha_i}{\alpha_{Fe}} \cong \frac{H_R^{Fe}}{H_R^i} \frac{\delta H_R^i}{\delta H_R^{Fe}}, \tag{4}$$

with H_R^i and δH_R^i standing for the resonance and linewidth field of the ferrite-based nanoparticles, respectively. The estimated values are presented in Table I and one can conclude that the damping factor follows the linewidth behavior. Further, from these results we also calculated $f\tau_0$ which as expected, was found to be in the same range as those of the cobalt ferrite and maghemite nanoparticles. Those parameters would be of extreme importance in the dynamic hysteresis simulations presented in section IV.

III. MAGNETO-HYPERTHERMIA

The magnetic hyperthermia experimental set up consists basically of a power supply, a coil (inductor) and a capacitor network (refrigerant cooled – 218nF), that together with the inductor (L-match) forms a resonant circuit. In our system the working frequency was around 500 kHz and corresponds to a sinusoidal wave. The copper coil length was 10.2 cm with a diameter of 2.2 cm. During the experiment the coil was cooled using a closed-loop circulating water system. At our experimental conditions the coil temperature is maintained at room temperature within an error of 0.3°C. Measurements were performed in an interval of 300s. In addition, the amplitude of the alternating magnetic fields was 45, 68, 90, 113 and 134Oe, obtained from measurements using an ac field probe bought from AMF lifesystems. The samples always had the same mass (0.090 ± 0.001 g) and were always inserted inside the coil at the same position. The sample container is made of polyethylene and was always the same. The container is open and we measure the temperature of the surface sample with an infrared meter. A data acquisition system converts the analogical signal from the infrared meter to a digital one that is then analyzed in a computer. In this section we start, firstly, discussing the main differences between the cobalt-ferrite and maghemite samples. Later in the text we compare both data with the other ferrite-based nanoparticles.

Figure 5(a) shows the temperature variation (ΔT) as a function of the measuring time for all values of the applied magnetic field amplitude; cobalt ferrite is shown in solid lines and maghemite in dashed. As expected, the higher the magnetic field the higher the temperature variation for all powder samples. Nevertheless, an interesting phenomenon can be observed from the data. At the low field range maghemite nanoparticles heat more, while at larger fields the cobalt ferrite samples achieves higher temperatures. Moreover, also at large fields, the temperature of the cobalt ferrite

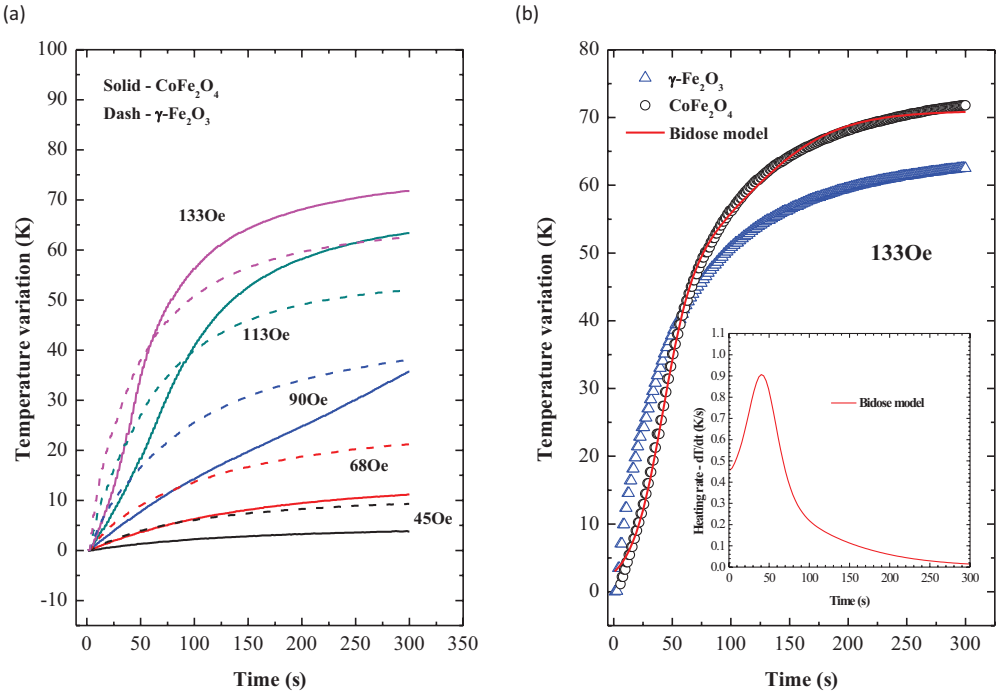

FIG. 5. (a) Temperature variation data for cobalt ferrite (solid lines) and maghemite (dashed lines) for different values of the applied field amplitude. (b) Temperature variation data for cobalt ferrite (circles) and maghemite (triangles) together with a bidose fit (solid line) for a field of 133Oe; (inset) heating rate time dependence obtained from the bidose fit.

samples is initially lower than that of maghemite. However, after some time, it starts to produce more heat, eventually crossing over the temperature profile of maghemite (see Fig. 5(b) for detail). Indeed, an analysis of the time dependence of the cobalt ferrite temperature suggests two different heating rates, while the same is not observed for the maghemite samples.

The SAR is obtained by the following equation: $SAR = (cM/m)(dT/dt)$, where c is the sample specific heat (assumed the same as the bulk value),[15] M is the total mass of the sample (in kg) and m is the mass of magnetic nanoparticles (in grams). Usually the initial linear slope of the sample temperature profile (dT/dt) is obtained by fitting the experimental data at the short time interval. Alternatively, one may use a Box-Lucas fitting procedure for the whole time dependence of the temperature profile and extract the heating rate in the short interval limit. We found similar heating rates using both procedures for the maghemite samples, which showed only a single heating rate. However, for the cobalt ferrite samples, at the higher field range, another procedure had to be introduced. Note that initially the heating rate of the cobalt ferrite sample is lower than maghemite (see for example Fig. 5(b)). However as time passes the heat generated by the cobalt sample crosses over the maghemite temperature profile, achieving higher temperatures at similar fields. Therefore using the initial slope certainly would not be in agreement with the experimental results, which showed, at the end, higher temperatures for the cobalt ferrite sample. In fact, recently Bordelon *et al.* pointed out that the previous procedure (initial or Box-Lucas) fails to yield the correct SAR at high-field amplitudes.[36] Moreover, the authors proposed to extract the heating rate from the analysis of the difference between subsequent recording temperatures at a given time range. Here we propose a similar approach but, instead of using the experimental data directly, we first fit the profile with a Bidose equation and then differentiate the fitted curve. This is intended to avoid the propagation of round-off errors, which could become considerable when taking finite differences of data. The inset in Fig. 5(b) shows the results (dT/dt) as a function of time. As previously suspected from the data analysis, we found two different heating rate behaviors. In our analysis we considered the maximum value as a better estimate for the SAR. Clearly, such ambiguity emphasizes the need for more robust approaches to estimate the SAR of high anisotropy samples.

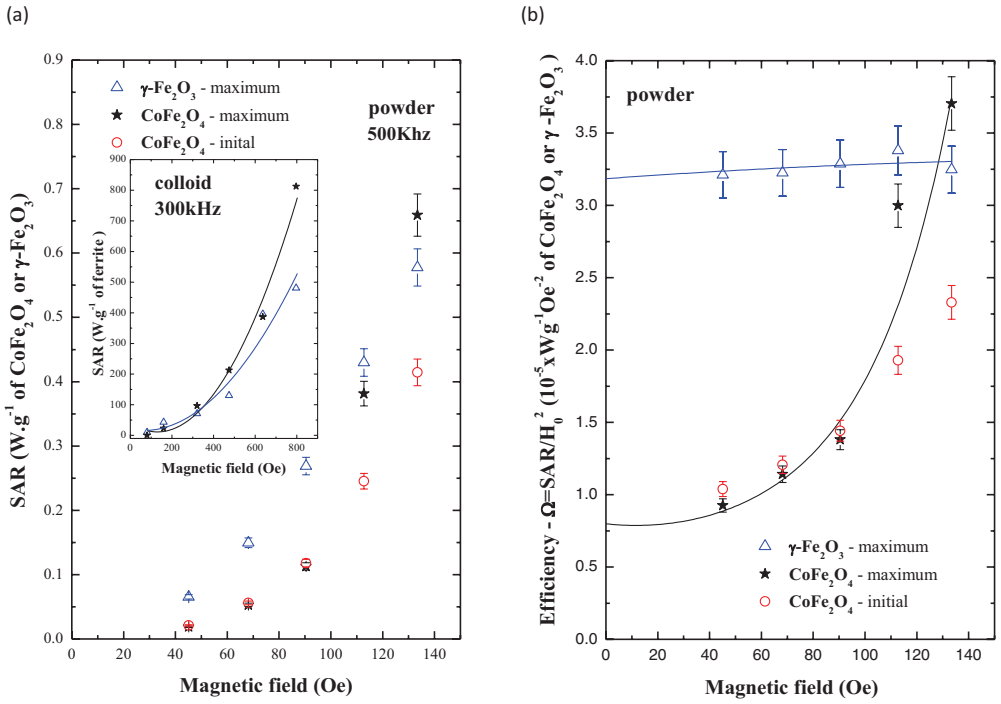

FIG. 6. (a) SAR vs. applied field amplitude for the powder cobalt ferrite (asterisks) and maghemite samples (open triangles) at 500kHz using the bidose model. Also shown is the SAR for cobalt ferrite estimated from the initial slope (open circles). In the inset we present SAR as function of magnetic field for both colloidal samples at higher field amplitudes and lower frequency (300kHz) (b) Efficiency, $\Omega = SAR/H_0^2$ vs. the applied field amplitude.

Fig. 6(a) shows the SAR as function of the magnetic field for both powder samples. The Bidose procedure was used for both samples, maghemite (triangles) and cobalt ferrite (asterisks). We also include the SAR calculated using the initial slope (circles), simply to illustrate that it completely disagrees with the experimental results, since it predicts a smaller heat generation. As can be seen, the SAR for cobalt ferrite starts to increase significantly at higher fields, finally surpassing that of maghemite at$\sim$133Oe. It thus becomes clear the existence of two distinct regimes, namely a low field regime where maghemite heats more and a high field regime where the inverse is true.

In addition, we also measured the SAR for the colloid samples. We found for the maghemite colloid a value of 47.0 W/(g of γ-Fe_2O_3) for the largest field (133Oe), which may be compared with 0.64 W/(g of γ-Fe_2O_3) for the powder sample (measured at a frequency of 500kHz). Similiar results regarding the relative scaling of the SAR between powder and colloidal systems were obtained for the cobalt-ferrite samples for all fields investigated. Dynamic light scattering was performed in the colloidal samples using a Nano-ZS Malvern system. The cobalt-ferrite (maghemite) based magnetic colloid had a hydrodynamic diameter of 170 nm (214 nm) with a PDI of 0.391 (0.290), while the zeta potential was +14.7 mV (−15.8 mV). Since, data on magnetic colloids are usually reported at higher magnetic fields, we also performed additional measurements using a commercial hyperthermia equipment system (model EasyHeat bought from Ambrell) that works at higher amplitude fields and lower ac magnetic field frequency. In the inset of Fig. 6(a) we show the SAR as function of the magnetic field for both magnetic colloid samples. One can observe, similar to the powder results, that at lower fields the SAR values of the cobalt ferrite is lower than maghemite but above a critical field the opposite is observed. Interesting the SAR value at 797 Oe of the cobalt ferrite colloid was found to be 813 W/g, while for the maghemite sample we found a lower value of 481 W/g. Those values are similar to others reported in the literature, and clearly corroborate the hyperthermia potential of cobalt-ferrite based nanostructures (if, through surface modification/passivation, it is possible to reduce or inhibit toxicity issues).

In passing, we note that the SAR values of the powder samples are much lower than their colloidal counterparts. Besides the fact that the SAR value is inversely proportional to the mass of ferrite content (which for powder equals the sample mass) and since the liquid sample has higher specific heat values the reason for such discrepancy is also related to the partial alignment of the nanoparticle easy axis in the fluid, in other words has to do with a less efficiency heating for such configuration. It is not difficult to understand that, when dispersed in liquid, the nanoparticles are allowed to rotate physically in response to the field (Brownian relaxation), whereas in powder only the rotation of the magnetic moment is allowed (Néel Relaxation). Thus, one expects a more easy-axis oriented system in the former and a randomly oriented system in the latter. In this case the theory predicts a smaller hysteresis loop area for randomly oriented arrangements and, as a consequence, a lower SAR. In addition, demagnetization effects might also be responsible for contributing to such differences.[37] Despite the importance of analyzing magnetic colloids, where particle concentration, molecular coating and nanoparticle self-organization might be extremely important (a full analysis of such parameters will be published elsewhere), let us return to the main discussion of this paper which tries to explain the differences reported between the powder samples.

The reason why we observe such marked differences between maghemite and cobalt ferrite is clearly related to the role of the magnetic anisotropy in the transition from the linear to the non-linear regime. Thus, let us analyze the data in Fig. 6(a) from the viewpoint of the efficiency, defined in Sec. I as $\Omega = SAR/H_0^2$ and shown in Fig. 6(b) (the solid lines are simply a guide to the eye). As can be seen, at very low fields (< 40Oe), Ω is roughly constant indicating that both samples are in the linear regime, with maghemite presenting a higher efficiency than cobalt ferrite (i.e., being a better heating center). Moreover, for the field range studied, the efficiency for both samples increase with H_0, which is now readily interpreted as the gradual departure towards the non-linear regime. However, cobalt ferrite presents a much steeper increase, eventually surpassing maghemite. Thus, according to the discussion in Sec. I, we expect that the higher anisotropy of cobalt ferrite entails a value of σ far into the high barrier regime. For maghemite, on the other hand, Ω is constant within the experimental error bars. This strongly suggests that this particle is more likely to be in the linear regime. Nevertheless, after comparing this result with the data from the others ferrites, it will become clear that this nanoparticle might has a slightly positive slope (thus also being in the high barrier regime) with a value of σ considerably smaller than that of cobalt ferrite. Unfortunately, quantifying the actual value of σ for each sample is not trivial, for the polidispersion of the samples and the interparticle interactions are expected to play a decisive role. We retake this discussion in Sec. V also inclusing the other ferrite-based nanoparticles data. For now, let us turn to theoretical simulations.

IV. DYNAMIC HYSTERESIS SIMULATIONS

We employ numerical simulations of dynamic hysteresis in an attempt to describe the transition to the non-linear regime. A robust method to simulate dynamic hysteresis under an arbitrary field is the Stochastic Landau-Lifshitz equation, which describes the time evolution of the magnetization vector **M**(t):

$$\frac{d\boldsymbol{M}}{dt} = -\gamma \boldsymbol{M} \times \boldsymbol{H}_{eff} - \frac{\alpha\gamma}{M_s} \boldsymbol{M} \times \left(\boldsymbol{M} \times \boldsymbol{H}_{eff}\right), \tag{5}$$

where $\boldsymbol{H}_{eff}$ is the effective magnetic field, comprising the external, anisotropy and thermal fields. The latter is introduced to account for the temperature dependence and, as customary, is taken as a Gaussian white noise random term.

The underlying assumption of this model is that the particles are in a single-domain state, whose dominant mode of magnetization reversal is coherent rotation. Fortunately, the size of the particles studied are precisely within this range; that is, they are neither too small for quantum effects to become important, nor too large for incoherent reversal or domain nucleation to become energetically favorable. However, in our simulations it was necessary to neglect particle-particle interactions, even though they are expected to be relevant in the samples considered. The reason for this is that the long-range nature of the dipolar interaction renders this problem computationally prohibitive.

Eq. (5) is a stochastic differential equation describing the time-evolution of the magnetization vector of each particle, which is now a random variable. The response of the sample (ensemble) is obtained by averaging over the stochastic realizations. The solution method employed was developed in Ref. 38 and enables for highly efficient and accurate calculations. It may also be used to compute the relaxation time exactly, whenever one requires higher accuracy than that provided by the Néel-Brown formula. We also refer the reader to Refs. 39 and 40 for an alternative solution method stemming from the same model and to Ref. 19 for a different approach based on transition state theory. For definiteness, we restrict our calculations to the ideal case where the field is parallel to the easy axis of the particles. Albeit being clearly an approximation, this assumption is known to yield qualitatively correct results. The main reason for this choice is that the number of parameters involved in the calculations reduce to: the field amplitude $h_0 = H_0/H_A$, where $H_A = 2K_{eff}/M_s$; the frequency f, given in units of $\tau_0 = (1+\alpha^2)/(\alpha\gamma_0 H_A)$; and $\sigma = K_{eff}V/k_BT$. Estimates of these parameters are given in Table I. From the hysteresis loop area (A), the SAR is computed simply as the product fA. To translate the simulated results to real values it is only necessary to multiply A by $M_s H_A$.

It is beyond the scope of this paper to use the simulations to "fit" of the experimental data. For this one would need to first consider an average over arbitrary oblique fields to account for the random orientation of the anisotropy axes, plus a second average over different values of σ due to the polidispersivity. Moreover, the entirety of the discussion would change due to inter-particle interactions and, finally, there remains the significant uncertainty in several parameters, τ_0 in particular. On the contrary, our goal is merely to qualitatively illustrate some general properties irrespective of such complexities.

The different values of τ_0 for each sample becomes of particular importance when we consider that the frequency response of the magnetization depends on the quantity $f\tau_0$, estimated in Table I. Albeit being seldom emphasized in the literature, this indeed has a profound effect on the magnetization dynamics. In Figs. 7 and 8 we present hysteresis loops for $f\tau_0 = 10^{-4}$ and 10^{-2}, respectively, for different values of σ and h_0. We note that, as asserted by more detailed simulations, $h_0 = 0.02$ accurately coincides with the linear regime response. The cobalt ferrite sample ($f\tau_0 = 0.2x10^{-4}$) is more closely represented by $f\tau_0 = 10^{-4}$, shown in Fig. 7, where the transition to the non-linear regime is clearly observed. The loops have a maximum area close to $\sigma \sim 10$, in agreement with the condition $f\tau \sim 1$ for this value of τ_0. At $f\tau_0 = 10^{-2}$ (Fig. 8), which is more representative of the maghemite sample ($f\tau_0 = 0.3x10^{-2}$), the influence of the anisotropy is significantly hindered by the high value of τ_0. The loops retain a quasi-elliptical shape reminiscent of the linear regime, with the area being a maximum at $\sigma \sim 4$. The deviations from the linear regime are thus much smaller, being expected to occur only at higher fields.

In Fig. 9 we present results for Ω vs. σ for different values of $f\tau_0$ and h_0 ranging from 0.02 (higher; darker) to 0.2 (shorter; lighter) in steps of 0.02. As $f\tau_0$ changes, the overall response is shifted towards higher values of σ while simultaneously increasing in magnitude. As can be seen, for $\sigma > \sigma_{max}$ all curves lie above the linear response curve whereas the opposite takes place at the complementary interval. Thus, as discussed, the efficiency increases (decreases) in the high (low) barrier regime. Also, as noted above, for $f\tau_0 = 10^{-2}$ the deviations from the linear behavior remain small, even at $h_0 = 0.2$. Finally, we call attention to the fact that the relative height between curves for different values of $f\tau_0$ is much smaller at $h_0 = 0.2$ than at $h_0 = 0.02$.

In Fig. 10 we present results for the SAR and the efficiency as a function of h_0 for three values of $f\tau_0$, focusing on values of σ close to the maximum condition $f\tau \sim 1$. Note that increasing $f\tau_0$, as shown in Fig. 9, one observes a drift of σ_{max} to larger values. These curves corroborate our previous discussion that one should expect the efficiency to increase (decrease) in the high (low) barrier regime. It also clearly shows, as does Fig. 6, that using the efficiency to analyze the data is much more productive than the SAR. One should also keep in mind that this indicates that for constant magnetic anisotropy values one can shift the maximum heating particle size to lower diameters, which can be much more useful for biomedical applications whenever colloidal stability plays a role. In this case a less degree of nanoparticle agglomeration is expected, that could be important in avoiding possible embolization issues.

In Fig. 11 we show 3D graphs of both the (a) SAR and (b) the efficiency versus (σ, h_0), with $f\tau_0 = 10^{-2}$. Here red and blue denote, in arbitrary units, large and small quantities respectively. The

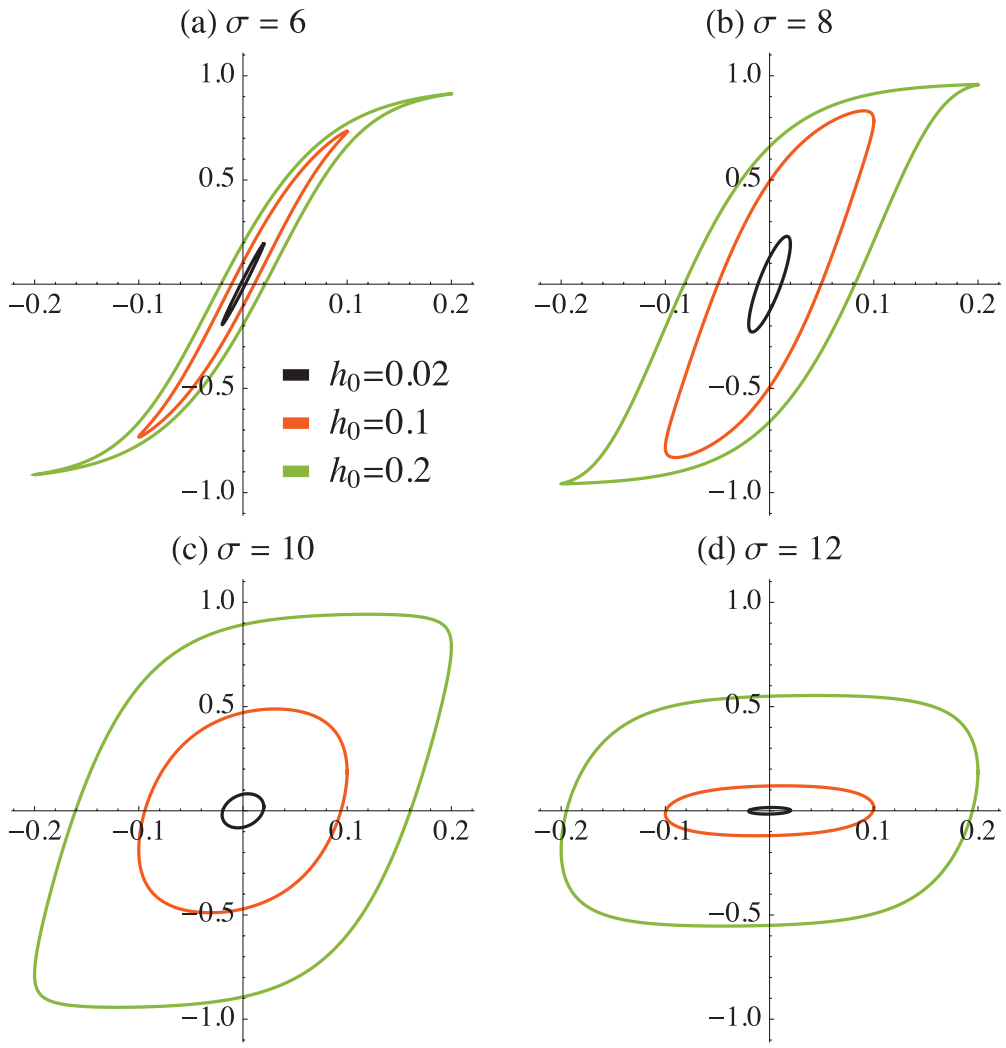

FIG. 7. Dynamic hysteresis simulations for different values of σ and $h_0 = H_0/H_A$, with $f\tau_0 = 10^{-4}$.

SAR is obviously maximum at large σ and h_0. However, while at low σ it gradually increases with h_0, at high σ it remains negligible until very high fields, above which it rapidly grows; this marks the field required to "unfreeze" the magnetization. The efficiency, on the other hand, is seen to achieve its maximum value at the linear response ($h_0 \to 0$). As the field increases, Ω is broadened and its peak simultaneously shifted to higher values of σ; this is in agreement with Fig. 9, which may be interpreted as slices of Fig. 11(b) for different values of h_0. At this point, it is worth emphasizing the crucial importance of the biological constraints pertaining to such applications. In particular, for a fixed frequency, the field amplitude must remain below a critical field value to inhibit eddy currents inside the patient body. Therefore, it is not a matter of just increasing the anisotropy of the nanoparticles as well as the applied field (which is also extremely troublesome at high frequencies) but, instead, looking towards the most efficient magnetic anisotropy for hyperthermia. So, from the simulations one can easily conclude that for fixed frequency and field values there will always be an optimum anisotropy parameter for the magneto-thermal application. Indeed, from Fig. 11, considering limited field values, two particular regions where no significant heat is produced: (i) at the very low barrier regime, i.e. for particles that are so small that, even at high frequencies, they do not present hysteresis [those might be named real superparamagnetic particles]. This is true even for the experimental maghemite sample that could be classified as a quasi-static superparamagnet. However, at the experimental frequency, several particles from the sample were in fact at the blocked

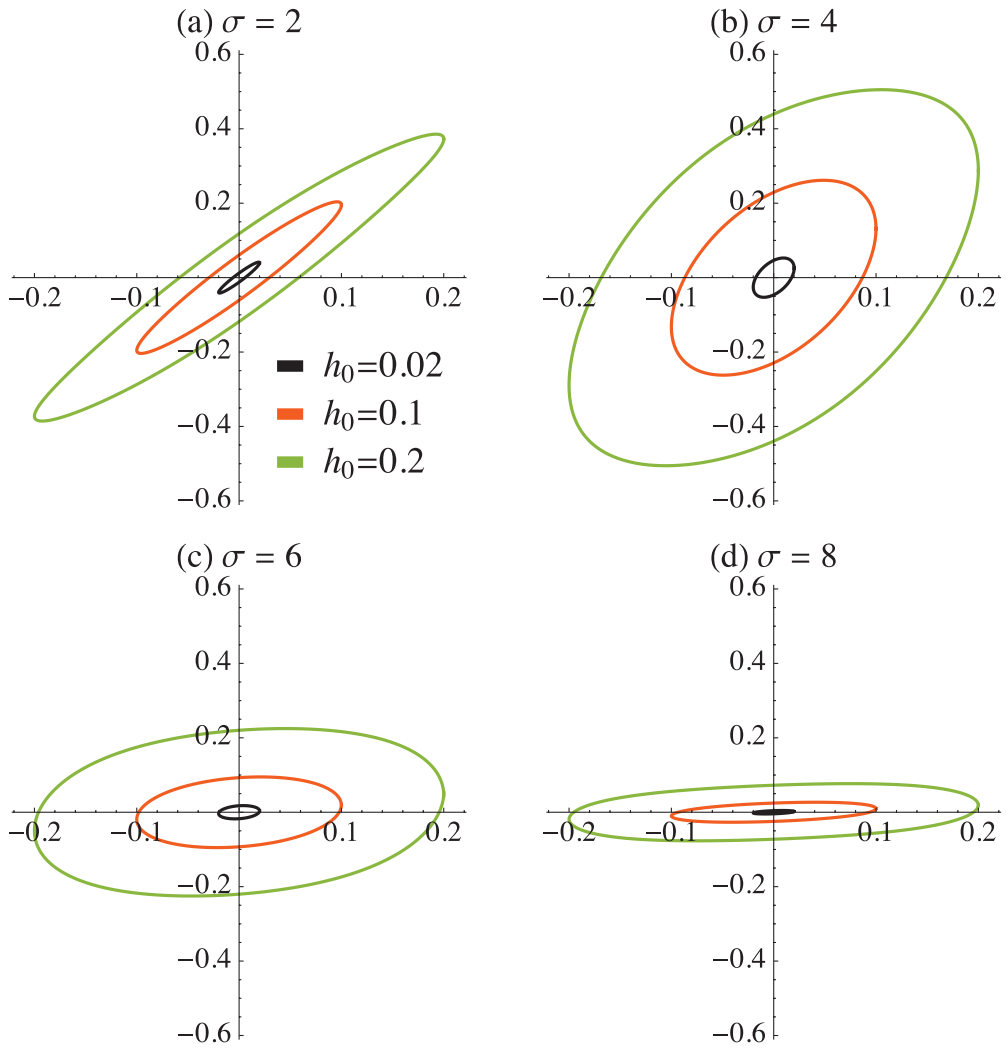

FIG. 8. Similar to Fig. 5 but for $f\tau_0 = 10^{-2}$.

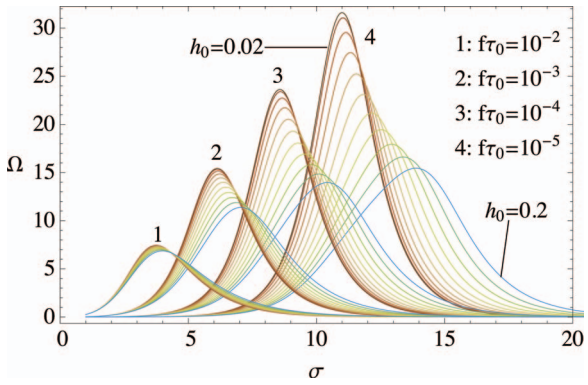

FIG. 9. Dynamic hysteresis simulations of the efficiency (Ω) vs. σ for different values of $f\tau_0$ and $h_0 = H_0/H_A$. The latter ranges from 0.02 (higher; darker) to 0.2 (shorter; lighter) in steps of 0.02.

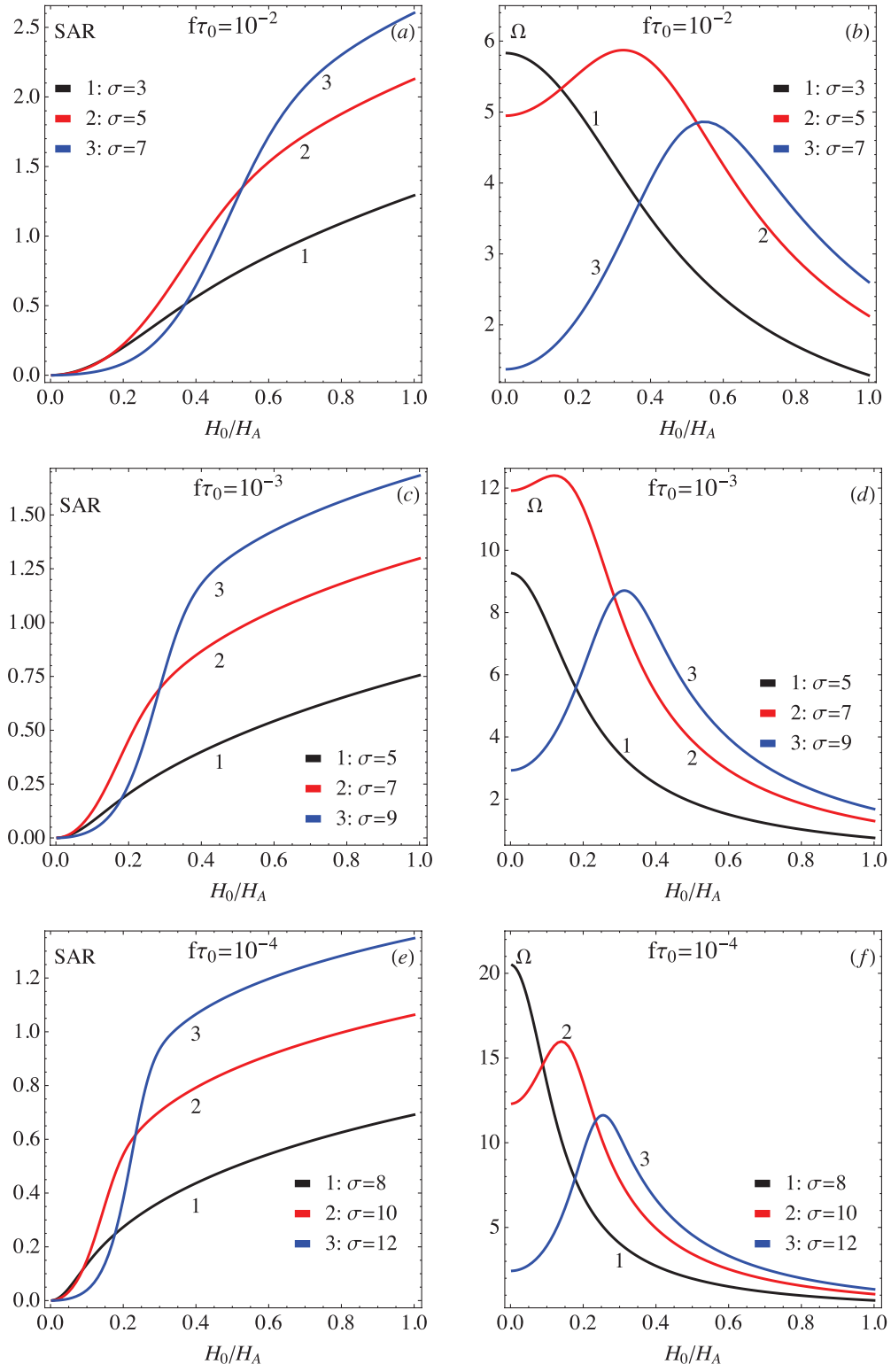

FIG. 10. Simulated SAR and efficiency vs. the applied field amplitude for different values of σ. (a) and (b) $f\tau_0 = 10^{-2}$ and $\sigma = 3$, 5 and 7.(c) and (d) $f\tau_0 = 10^{-3}$ and $\sigma = 5$, 7 and 9. (e) and (f) $f\tau_0 = 10^{-4}$ and σ =8, 10 and 12.

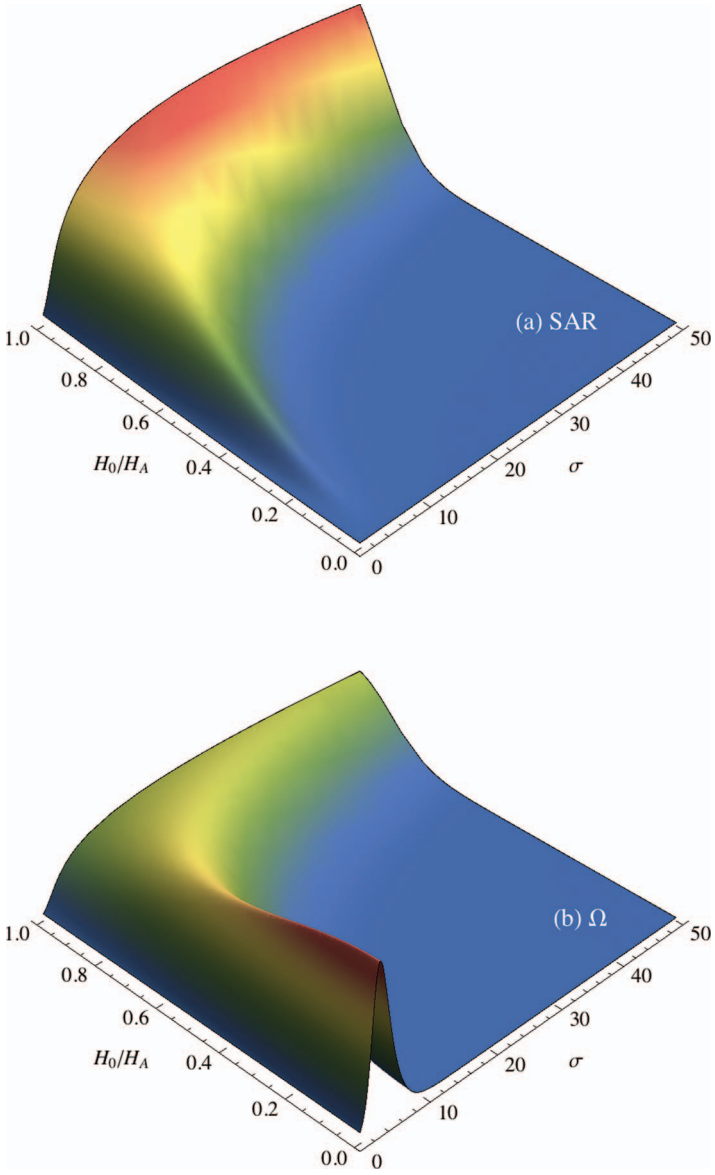

FIG. 11. Simulated (a) SAR and (b) efficiency vs. (σ, h_0), with $f\tau_0 = 10^{-2}$.

state, showing hysteresis and promoting heat. Indeed, experimental confirmations of this effect had already been published;[16] and (ii) at the very high barrier region, where the anisotropy is so high that only extremely (perhaps even unrealistic) fields are required to promote efficient spin reversals.

V. INTERPARTICLE INTERACTIONS

In Sec. I we claimed via heuristic arguments, that an increasing (decreasing) efficiency implied particles in the high (low) barrier regime. Accordingly, the main assertion regarding Fig. 6(b) is that the steeper increase in the efficiency for the cobalt ferrite sample is a signature of its higher anisotropy value; that is, it requires larger field amplitudes to "unfreeze" the magnetic moments. These claims are visibly endorsed by the dynamic hysteresis simulations presented in Figs. 7–11. However, we do not expect any quantitative agreement due to the vast simplifications concerning the latter (or, alternatively, the inherent complexities of the former). Indeed, some of the estimates in Table I are clearly inconsistent. For instance, from the aforementioned arguments we'd expect

an increasing efficiency when $\sigma > \sigma_{max}$. The latter is determined by the condition $f\tau = 1$ and is estimated in Table I for different values of τ_0. As can be seen, the estimates for σ are smaller than $\sigma_{\max}$ in all cases, the only exception being that of cobalt ferrite under the assumption of bulk anisotropy. Clearly, this contradicts the positive slope observed in Fig. 6(b). As we now discuss, despite the uncertainties pertaining to the experimental data, we believe that interparticle interactions have a decisive role on this discussion, for they are expected to increase the effective value of σ.

Owing to the long-range nature of the dipolar field, such analysis is well known to be quite troublesome. Notwithstanding, one may at least discuss it qualitatively. For instance, it is known from the literature that, in general, the stronger the interaction the higher the effective energy barrier, *i.e.*, $\sigma_{eff} = \sigma + \sigma_{dip}$, with $\sigma_{dip} > 0$. A possible theoretical approach to estimate σ_{dip} is the DBF model,[41] which yields for the regime of strong interactions

$$\sigma_{dip} = \frac{n_1 \pi^2 M_S^2 d^3}{36kT}, \tag{6}$$

where n_1 is the number of first neighbors. According to Ref. 30, a good estimate is $n_1 = 10$. In Table I we present estimates of this parameter for both samples. Clearly, the increase in σ_{eff} helps justify, at least qualitatively, the differences between experiment and simulations (cf. Figs. 6 and 10). Indeed, taking into account interparticle interactions, our estimates of σ_{eff} for cobalt ferrite are modified to lie roughly between 7.2 to 26.2, precisely within the high-barrier regime of the dynamic hysteresis simulations (cf. Figs. 10(e) and 10(f)). Similarly, for maghemite we found values between 2.5 to 9.8, which are also close to those in Figs. 10(a) and 10(b). The estimations above were performed assuming a monodisperse system. The values increase considerably when size dispersity is taken into account (see the same values in brackets in Table I). For example, for the cobalt-ferrite sample σ_{eff} changes from 7.2 to 13.7. In fact, for $f\tau_0 = 10^{-5}$ the threshold σ is roughly 11.5, above which one should already observe nanoparticles in the high barrier regime. Therefore, we conclude that interparticle interactions are indeed expected to play a key role in the experimentally observed increase of the efficiency, as presented in Fig. 6(b). Nevertheless, for maghemite, even taking size dispersity into account one is not able to explain the experimental data, as a consequence a more sophisticated model might be needed. This becomes more clear when other ferrite-based nanoparticles are investigated.

VI. DIFFERENT FERRITE-BASED NANOPARTICLES

Fig. 12(a) shows the SAR as function of magnetic field amplitude for all ferrite-based nanoparticles. In the inset we also show the time dependence of the temperature variation for all powder samples at 133Oe and 500kHz. From these results it is quite apparent that, at this field conditions, cobalt-ferrite is the best magnetic heating material. Conversely, at the low field regime, maghemite and copper-ferrite become the best materials. These conclusions suggest a solid strategy to optimize the heating properties for different experimental conditions. The importance of such analysis becomes evident when one considers the fundamental role that adequately choosing the field amplitude and frequency may have in inhibiting undesirable eddy currents inside the body. We will return to this point later in the text.

Fig. 12(b) presents the efficiency (SAR/H_0^2) versus the magnetic field amplitude. As before, it is seen to display a broad range of interesting behaviors. Now, instead of only increasing with the magnetic field amplitude, the efficiency may also decrease, as well as present a maximum. So, in summary, we must: (a) answer why at the high field range the SAR is higher (lower) for the cobalt-ferrite (zinc-ferrite and copper-ferrite); (b) what governs the behavior of the efficiency, i.e. why should it decrease or present a more complex feature. Those questions can be answered in a qualitative way by comparing the experimental data with our dynamic hysteresis simulations (see Fig. 10).

From the SAR theoretical analysis, at the high field limit, as function of the anisotropy parameter σ (Table I) we expected the following order: Co > Ni > Fe > Zn > Cu. According to Fig. 12(a) we found: Co > Fe > Ni > Cu > Zn. In addition, the concepts discussed in sections I and IV may be

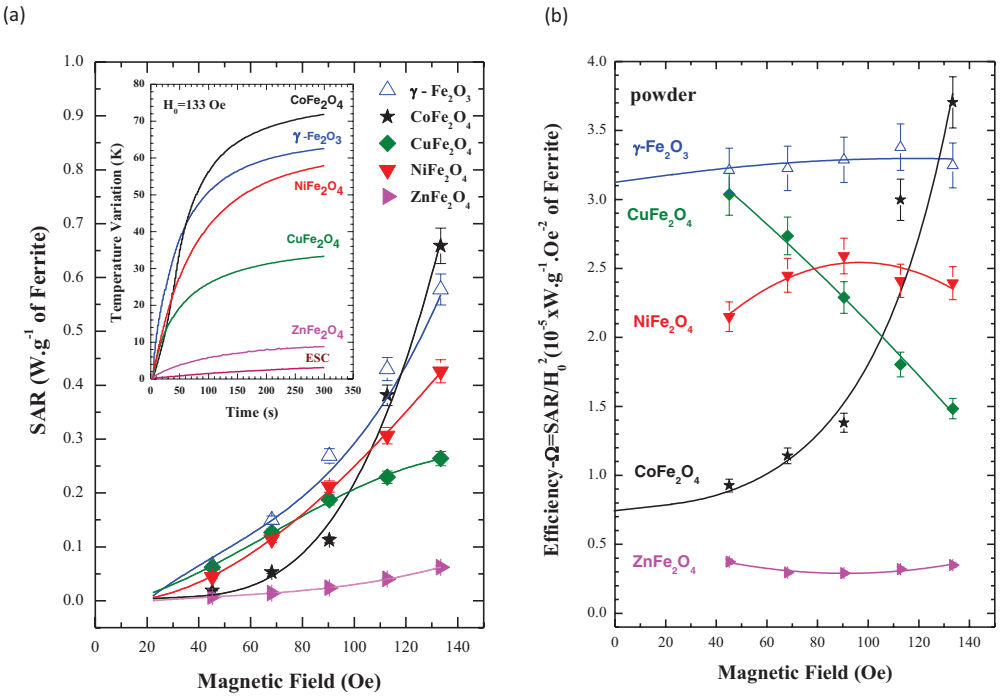

FIG. 12. (a) SAR vs. applied field amplitude for the powder of ferrite-based nanoparticles (symbols) at 500kHz. The solid lines are just guide to the eye. In the inset we present temperature variation data as function of time for all the samples for a field of 133Oe. (b) Efficiency, $\Omega = SAR/H_0^2$ vs. the applied field amplitude for all the ferrite-based nanoparticles. Symbols represent experimental data, while the solid lines are just guide to the eye.

readily employed to analyze the efficiency in Fig. 12(b). In these terms, it is possible to claim that the cobalt-ferrite, nickel-ferrite and maghemite samples are in the high barrier regime with respect to 500 kHz. Conversely, copper-ferrite and zinc-ferrite are clearly in the low barrier regime. As already stated before, unfortunately, the values obtained for σ_{eff} seems to be lower than the ones expected theoretically, especially for nickel-ferrite and maghemite. Although, from Fig. 12(b), it is clear that the Ni-ferrite nanoparticle is at the high-barrier regime. Note, so far, that all the discussed parameters reported so far were calculated assuming a homogeneous nanoparticle. Nevertheless, in section II, it became clear that, due to surface passivation, those nanoparticles are more likely to be represented as a core-shell nanostructure. Therefore, in order to check if this hypothesis could better explain our experimental data similar calculations were performed now taking into account both, core-shell structure as well as size dispersity. Curiously, only few parameters change in this model, namely the magnetic anisotropy and the dipolar anisotropy term, while the characteristic time τ_0 remains unchanged (compare the values in Tables I and II). This occurs because the increase in the effective anisotropy is modulated by the different magnetization value in such a way that the anisotropy field (which is the ratio between the magnetic anisotropy to the magnetization) remains the same. So in the core-shell model one, firstly, use the value of the shell thickness κ estimated from the CS-Magn. procedure (see section II), with the main objective to estimate the modal particle size $^*D_{MODAL}$ (which is equivalent to the experimental D_{TEM}) and assuming the average dispersity value $^*\delta_D = 0.25$. Further, because of the weakly magnetic shell structure the effective dipolar barrier σ_{dip-CS} is now calculated in the regime of strong interactions as

$$\sigma_{dip-CS} = \frac{n_1\pi^2(M_S^{core})^2 D_{RR}^6}{36kT\,D_{modal}^3} = \frac{n_1\pi^2(M_S^{core})^2 D_{RR}^3}{36kT(1+2\kappa/D_{RR})^3}. \quad (7)$$

In Table II is shown the same parameters as before now taking into account a core-shell structure with size dispersion (It was assumed the same dispersity for the core diameter). One can notice that

the effective anisotropy barrier had increased when compared with the previous calculation (see Table I). However, for nickel-ferrite the value is still in the low-barrier regime in contradiction with the experimental data. Nevertheless, considering a higher size dispersity, as for instance 0.30 (values in brackets in Table II) one obtain a value already at the highe-barrier regime. So we conclude that probably this sample has a higher dispersion parameter than cobal-ferrite and the maghemite nanoparticle.

So, as can be seen in Table II the average initial slope of the efficiency is almost in full agreement with the values of σ obtained for each sample. On the other hand, from the efficiency (Ω) analysis one would expect in the low field limit, $\Omega(H \rightarrow 0)$, a maximum as function of σ. Indeed this is observed for nickel-ferrite. So we expect such behavior, at higher fields, for both cobalt-ferrite and probably also for the maghemite nanoparticle. Moreover, one can clearly understand why cobalt at low fields has a lower efficiency in comparison with nickel-ferrite as well as the maghemite sample. The only discordance with our analysis might be the comparison between copper and zinc-ferrite. As discussed before, may be the inclusion of polidispersity effects (or surface anisotropy)[24–26] could explain those discrepancies.

Further, there are several interesting works in the literature regarding the use of magnetic nanoparticles for magnetic hyperthermia. Most of them, however, are based on magnetite/maghemite structures, although there are other types of ferrite reported. However in most cases no detailed comparison between those materials are made. The exceptions are the work from Maehara *et al.*,[42] who investigated seven types of ferrites but (unfortunately) at the micrometer range, Jeun *et al.*[43] that reported hyperthermia studies with particles around 30 nm of three ferrites, namely Co, Ni and Mg-based ones, and within the same size range of this investigation the interesting work of Lee *et al.*[44] which reported data on Co, Fe and Mn-based ferrites as well as exchange-coupled crystalline core-shell (hard-soft magnetic) nanostructures. Nevertheless, it is known that larger particle sizes might be influenced by incoherent rotation (curling/vortex-like for soft magnets) or domain-wall motion, which need to be correctly modeled in order to make a fair comparison with experimental data. Not less important, at such large sizes particle agglomeration, lower tumor permeability retention effects[45] and/or colloidal stability issues might not be so easily or safely controlled for real biomedical applications. Those problems might be minimized at the particle size investigated in this work. The fact that, at this diameter range, coherent rotation is probably a good approximation (for nanoparticle sizes and types where surface spin disorder is not so relevant) allowed us to give a good insight about the important parameters (not forgetting the particle size) involved in magnetic hyperthermia phenomena, namely the saturation magnetization (relevant also to the effective anisotropy energy due to dipole-dipole interactions), magnetic anisotropy and not less important the damping parameter which can play an important role in the characteristic relaxation time.

Finally, as far as we know, the first measurements confirming high frequency hysteresis effects in magnetic colloids (designed for magnetic hyperthermia applications) were only reported recently.[16] In addition, real comparison between frequency hysteresis measurements and dynamic hysteresis simulations were only now confronted (see Refs. 37 and 46). It was proved that: (i) SAR measurements are intimately related to the dynamic hysteresis area, as expected from theory (although some references in the literature seem, wrongly, to believe that "superparamagnetic" nanoparticles can heat); and that (ii) dynamic hysteresis simulations can reproduce, fairly well, real frequency dependent magnetic measurements.[46] Therefore, as our main objective was to make a qualitative comparison between our experimental results and dynamic hysteresis simulations, in order to give support to the important role of magnetic anisotropy and damping factor into the magneto thermal properties of the nanoparticles. From our point of view, the approach used here might be highly useful to the development of more efficient magnetic nanoparticles for biomedical applications, since it is able to represent several real magnetic hyperthermia features from the magnetic nanoparticles. On the other hand, in magnetic colloids the dipolar contribution to the effective magnetic anisotropy should be included. In this case it will be necessary to extract information about nanoparticle self-organization inside the fluid. Therefore, other experimental techniques such as magneto-optical ones[47,48] together with Monte Carlo simulations[49] might be needed. However, this is beyond the scope of the present investigation and will be left to another work.

VII. CONCLUSIONS

In this paper we provided a thorough investigation of the intimate relation between the magnetic anisotropy of the nanoparticles and the departure from the linear regime. As we have shown, whereas at low fields maghemite is a more efficient heating center, as the field increases and the magnetic moments of the cobalt ferrite nanoparticles are gradually unblocked, its heating power eventually surpasses maghemite as well as others ferrite-based nanoparticles. Dynamic hysteresis simulations using the stochastic Landau-Lifshitz model corroborate the experimental results and, coupled with simple heuristic arguments, provide useful guidelines for the analysis of the experimental data. In particular, we mention the use of the energy conversion efficiency, defined as the ratio between the power loss and the square of the field amplitude. It enables for powerful qualitative information to be extracted from a simple comparison between the different samples. From the efficiency data analysis we concluded that cobalt-ferrite, maghemite and nickel-ferrite were at the high barrier regime, probably due to interparticle interactions, while the opposite was found for copper-ferrite and zinc-ferrite. Indeed, the excellent qualitative agreement between the experiment and the simulations, endorsed by the biomedical constraints (due to the generation of eddy currents for high enough field frequencies and field amplitudes), confirm the existence of optimum magnetic anisotropy values. In addition, it also clearly indicates that superparamagnets, defined as particles that does not show hysteresis at the experimental frequency, as well as very hard magnetic materials, that showed no spin rotation for the experimental field amplitudes, do not generate heat. Finally, regarding our experimental findings, we conclude that for low magnetic field amplitude hyperthermia applications, copper-ferrite and maghemite nanoparticles are promising materials, while at the high field range cobalt-ferrite has the best magnetic hyperthermia properties at those experimental conditions.

ACKNOWLEDGMENTS

The authors would like to thank financial support from the Brazilian agencies CNPq, CAPES, FINEP, FAPEG, FAPESP, FAPDF and FUNAPE. We also thank LNLS for the X-ray and TEM of the maghemite sample.

[1] K. Yosida and M. Tachiki, Prog. Theor. Phys. **17**, 331 (1957).
[2] V. A. M. Brabers, Phys. Rev. Lett. **68**, 3113 (1992).
[3] C. R. Alves, R. Aquino, J. Depeyrot, T. A. P. Cotta, M. H. Sousa, F. A. Tourinho, H. R. Rechenberg, and G. F. Goya, J. Appl. Phys. **99**, 08M905 (2006).
[4] M. Verveka, Z. Jirak, O. Kaman, K. Knizek, M. Marysko, E. Pollert, K. Zaveta, A. Lancok, M. Dlouha, and S. Vratislav, Nanotechnology **22**, 345701 (2011).
[5] A. V. Ramos, M. J. Guittet, J. B. Moussy, R. Mattana, C. Deranlot, F. Petroff, and C. Gatel, Appl. Phys. Lett. **91**, 122107 (2007).
[6] H. Zheng, J. Wang, S. E. Lofland, Z. Ma, L. M. Ardabili, T. Zhao, L. S. Riba, S. R. Shinde, S. B. Ogale, F. Bai, D. Viehland, Y. Jia, D. G. Schlom, M. Wuttig, A. Roytburd, and R. Ramesh, Science **303**, 661 (2004).
[7] Y. Wu, J. G. Wan, J. M. Liu, and G. Wang, Appl. Phys. Lett. **96**, 152902 (2010).
[8] R. K. Gilchrist, R. Medal, W. D. Shorey, R. C. Hanselman, J. C. Parrot, and C. B. Taylor, Annals of Surgery **146**, 596 (1957).
[9] A. Jordan, R. Scholz, P. Wust, H. Fahling, J. Krause, W. Wlodarczyk, B. Sander, T. Vogl, and R. Felix, Int. J. Hyperthermia **13**, 587 (1997).
[10] M. H. A. Guedes, N. Sadeghiani, D. L. G. Peixoto, J. P. Coelho, L. S. Barbosa, R. B. Azevedo, S. Kückelhaus, M. F. Da Silva, P. C. Morais, and Z. G. M. Lacava, J. Magn. Magn. Mater. **293**, 283 (2005).
[11] A. Ito, H. Honda, and T. Kobayashi, Cancer Immunol. Immunother. **55**, 320 (2006).
[12] C. L. Dennis, A. J. Jackson, J. A. Borchers, P. J. Hoopes, R. Strawbridge, A. R. Foreman, J. van Lierop, C. Grüettner, and R. Ivkov, Nanotechnology **20**, 395103 (2009).
[13] F. F. Fachini and A. F. Bakuzis, J. Appl. Phys. **108**, 084309 (2010).
[14] W. Andrä, C. G. d'Ambly, R. Hergt, I. Hilger, and W. A. Kaiser, J. Magn. Magn. Mater. **194**, 197 (1999).
[15] R. E. Rosensweig, J. Magn. Magn. Mater. **252**, 370 (2002).
[16] A. S. Eggeman, S. A. Majetich, D. Farrel, and Q. A. Pankhust, IEEE Trans. Magn. **43**, 2451 (2007).
[17] K. M. Krishnan, IEEE Trans. Magn. **46**, 2523 (2010).
[18] I. Hilger, R. Hergt, and W. A. Kaiser, IEE Proc. Nanobiotechnology **152**, 33 (2005).
[19] J. Carrey, B. Mehdaoui, and M. Respaud, J. Appl. Phys. **109**, 083921 (2011).
[20] W. F. Brown, Jr., Phys. Rev. **130**, 1677 (1963).
[21] G. T. Landi and A. F. Bakuzis, J. Appl. Phys. **111**, 083915 (2012).

[22] M. H. Sousa, F. A. Tourinho, J. Depeyrot, and G. J. da Silva, J. Phys. Chem. B **105**, 1168 (2001).
[23] R. Itri, J. Depeyrot, F. A. Tourinho, and M. H. Sousa, Eur. Phys. J. E **4**, 201 (2001).
[24] A. F. Bakuzis, P. C. Morais, and F. A. Tourinho, J. Magn. Reson. **122**, 100 (1996).
[25] A. F. Bakuzis, P. C. Morais, and F. Pelegrini, J. Appl. Phys. **85**, 7480 (1999).
[26] V. P. Shilov, Y. L. Raikher, J. C. Bacri, F. Gazeau, and R. Perzynski, Phys. Rev. B **60**, 11902 (1999).
[27] H. G. Belgers and J. Smit, Philips Res. Rep. **10**, 113 (1955).
[28] J. G. Otero, A. J. G. Bastida, and J. Rivas, J. Magn. Magn. Mater. **189**, 377 (1998).
[29] B. D. Cullity and C. D. Grahan, *Introduction to Magnetic Materials* (John Wiley& Sons, New York, 2009).
[30] A. Donev, I. Cisse, D. Sachs, E. A. Variano, F. H. Stillinger, R. Connelly, S. Torquato, and P. M. Chaikin, Science **303**, 990 (2004).
[31] E. L. Verde, G. T. Landi, J. A. Gomes, M. H. Sousa, and A. F. Bakuzis, J. Appl. Phys. **111**, 123902 (2012).
[32] J. A. Gomes, M. H. Sousa, F. A. Tourinho, R. Aquino, G. J. Silva, J. Depeyrot, E. Dubois, and R. Perzynski, J. Phys. Chem. C **112**, 6220 (2008).
[33] R. H. Kodama, A. E. Berkowitz, E. J. McNiff, and S. Foner, Phys. Rev. Lett. **77**, 394 (1996).
[34] J. M. D. Coey, Phys. Rev. Lett. **27**, 1140 (1971).
[35] E. C. Sousa, M. H. Sousa, G. F. Goya, H. R. Hechenberg, M. C. F. L. Lara, F. A. Tourinho, and J. Depeyrot, J. Magn. Magn. Mater. **272-276**, e1215 (2004).
[36] D. E. Bordelon, C. Cornejo, C. Brüttner, F. Westphal, T. L. DeWeese, and R. Ivkov, J. Appl. Phys. **109**, 124904 (2011).
[37] S. A. Gudoshnikov, B. Ya. Liubimov, and N. A. Usov, AIP Advances **2**, 12143 (2012).
[38] G. T. Landi, J. Appl. Phys. **111**, 043901 (2012).
[39] I. S. Poperechny, Y. L. Raikher, and V. I. Stepanov, Phys. Rev. B **82**, 174423 (2010).
[40] N. A. Usov, J. Appl. Phys. **107**, 123909 (2010).
[41] J. L. Dormann, F. DÓrazi, F. Lucari, E. Tronc, P. Prené, J. P. Jolivet, D. Fiorani, R. Cherkaoui, and M. Noguès, Phys. Rev. B **53**, 14291 (1996).
[42] T. Maehura, K. Konishi, T. Kamimori, H. Aono, H. Hirazawa, T. Naohara, S. Nomura, H. Kikkawa, Y. Watanase, and K. Kawachi, J. Mater. Sci. **40**, 135 (2005).
[43] M. Jeun, S. Bae, A. Tomitaka, Y. Takemura, K. H. Park, S. H. Paek, and K. Chung, Appl. Phys.Lett. **95**, 082501 (2009).
[44] J. H. Lee, J. t. s. Jang, J. Choi, S. H. Moon, S. h. Noh, J. w. Kim, J. G. Kim, I. S. Kim, K. I. Park, and J. Cheon, Nature Nanotechnology **6**, 418 (2011).
[45] V. P. Chauhan, T. Stylianopoulos, J. D. Martin, Z. Popovic, O. Chen, W. S. Kamoun, M. G. Bawendi, D. Fukumura, and R. K. Jain, Nature Nanotechnology **7**, 383 (2012).
[46] B. Mehdaoui, J. Carrey, M. Stadler, A. Cornejo, C. Nayral, F. Delpech, B. Chaudret, and M. Respaud, Appl. Phys.Lett. **100**, 052403 (2012).
[47] M. T. A. Eloi, J. L. Santos, Jr., P. C. Morais, and A. F. Bakuzis, Phys. Rev. E **82**, 021407 (2010).
[48] E. R. Cintra, F. S. Ferreira, J. L. Santos, Jr., J. C. Campello, L. M. Socolovsky, E. M. Lima, and A. F. Bakuzis, Nanotechnology **20**, 045103 (2009).
[49] L. L. Castro, G. R. R. Gonçalves, K. Skeff Neto, P. C. Morais, A. F. Bakuzis, and R. Miotto, Phys. Rev. E **78**, 061507 (2008).